

The JCMT Legacy Survey of the Gould Belt: a first look at Serpens with HARP

S. F. Graves,^{1,2*} J. S. Richer,^{1,2} J. V. Buckle,^{1,2} A. Duarte-Cabral,³ G. A. Fuller,³
M. R. Hogerheijde,⁴ J. E. Owen,⁵ C. Brunt,⁶ H. M. Butner,^{7,8} B. Cavanagh,⁸
A. Chrysostomou,^{8,9} E. I. Curtis,^{1,2} C. J. Davis,⁸ M. Etxaluze,^{10,11} J. Di Francesco,^{12,13}
P. Friberg,⁸ R. K. Friesen,¹⁴ J. S. Greaves,¹⁵ J. Hatchell,⁶ D. Johnstone,^{12,13}
B. Matthews,¹² H. Matthews,¹⁶ C. D. Matzner,¹⁷ D. Nutter,¹⁸ J. M. C. Rawlings,¹⁹
J. F. Roberts,²⁰ S. Sadavoy,^{12,13} R. J. Simpson,¹⁸ N. F. H. Tohill,^{6,21} Y. G. Tsamis,²²
S. Viti,¹⁹ D. Ward-Thompson,¹⁸ G. J. White,^{10,11} J. G. A. Wouterloot⁸ and J. Yates¹⁹

¹*Astrophysics Group, Cavendish Laboratory, J J Thomson Avenue, Cambridge CB3 0HE*

²*Kavli Institute for Cosmology, c/o Institute of Astronomy, University of Cambridge, Madingley Road, Cambridge CB3 0HA*

³*Jodrell Bank Centre for Astrophysics, School of Physics and Astronomy, The University of Manchester, Oxford Road, Manchester M13 9PL*

⁴*Leiden Observatory, Leiden University, PO Box 9513, 2300 RA, Leiden, the Netherlands*

⁵*Institute of Astronomy, University of Cambridge, Madingley Road, Cambridge CB3 0HE*

⁶*School of Physics, University of Exeter, Stocker Road, Exeter EX4 4QL*

⁷*Department of Physics and Astronomy, James Madison University, 901 Carrier Drive, Harrisonburg, VA 22807, USA*

⁸*Joint Astronomy Centre, 660 N. A'Ohoku Place, University Park, Hilo, Hawaii 96720, USA*

⁹*School of Physics, Astronomy and Mathematics, University of Hertfordshire, College Lane, Hatfield AL10 9AB*

¹⁰*Science and Technology Facilities Council, Rutherford Appleton Laboratory, Chilton, Didcot OX11 0QX*

¹¹*Department of Physics and Astronomy, Open University, Walton Hall, Milton Keynes MK7 6BT*

¹²*National Research Council Canada, Herzberg Institute of Astrophysics, 5071 West Saanich Rd, Victoria, BC V9E 2E7*

¹³*Department of Physics & Astronomy, University of Victoria, 3800 Finnerty Rd., Victoria, BC, Canada*

¹⁴*North American ALMA Science Center, National Radio Astronomy Observatory, 520 Edgemont Rd, Charlottesville VA 22903, USA*

¹⁵*Scottish Universities Physics Alliance, Physics & Astronomy, University of St Andrews, North Haugh, St Andrews, Fife KY16 9SS*

¹⁶*National Research Council of Canada, Dominion Radio Astrophysical Observatory, 717 White Lake Rd., Penticton, BC, Canada*

¹⁷*Department of Astronomy & Astrophysics, University of Toronto, 50 St George Street, Toronto, Canada*

¹⁸*School of Physics & Astronomy, Cardiff University, 5 The Parade, Cardiff CF24 3AA*

¹⁹*Department of Physics & Astronomy, University College London, Gower Street, London WC1E 6BT*

²⁰*Centro de Astrobiología (CSIC/INTA), Ctra de Torrejón a Ajalvir km 4, E-28850 Torrejón de Ardoz, Madrid, Spain*

²¹*School of Physics, University of New South Wales, Sydney, NSW 2052, Australia*

²²*Instituto de Astrofísica de Andalucía (CSIC), Camino Bajo de Huífor 50, 18008 Granada, Spain*

Accepted 2010 June 2. Received 2010 April 30; in original form 2010 January 15

ABSTRACT

The Gould Belt Legacy Survey on the James Clerk Maxwell Telescope's has observed a region of 260 arcmin² in ¹²CO $J = 3 \rightarrow 2$ emission, and a 190 arcmin² subset of this in ¹³CO and C¹⁸O towards the Serpens molecular cloud. We examine the global velocity structure of the non-outflowing gas, and calculate excitation temperatures and opacities. The large-scale mass and energetics of the region are evaluated, with special consideration for high-velocity gas. We find the cloud to have a mass of 203 M_☉, and to be gravitationally bound, and that the kinetic energy of the outflowing gas is approximately 70 per cent of the turbulent kinetic energy of the cloud. We identify compact outflows towards some of the submillimetre Class 0/I sources in the region.

*E-mail: s.graves@mrao.cam.ac.uk

Key words: molecular data – stars: formation – ISM: jets and outflows – ISM: kinematics and dynamics – submillimetre: ISM.

1 INTRODUCTION

1.1 The JCMT Gould Belt Survey

The James Clerk Maxwell Telescope’s (JCMT) Gould Belt Legacy Survey (GBS) (Ward-Thompson et al. 2007) is a large-scale programme to observe nearby (<500 pc) regions of active star formation in both submillimetre continuum emission and three CO species $J = 3 \rightarrow 2$ emission.¹ The survey will observe molecular clouds with SCUBA-2 (Holland et al. 2006) to detect the continuum emission, and has been carrying out heterodyne spectrometer observations of filamentary regions in a subset of these clouds. These observations are currently being carried out with HARP/ACSIS (Buckle et al. 2009) in the ^{12}CO , ^{13}CO and C^{18}O isotopologues, in the $J = 3 \rightarrow 2$ transition. POL-2 (Bastien et al. 2005), the SCUBA-2 polarimeter, will also be used to study some of the SCUBA-2 observed regions. A first look at the data from the Orion-B region has already been presented, by Buckle et al. (2010), and from the Taurus region by Davis et al. (2010).

The survey seeks to perform some of the first large-scale analyses of very large, high-resolution submillimetre maps and data cubes of the closest molecular clouds and examine the star formation occurring within them. In particular, the spectral part of this survey will examine the properties of higher density gas than most large-scale surveys, due to the higher critical density of the $J = 3 \rightarrow 2$ transitions (10^4 – 10^5 cm^{-3}). This is better matched to the densities probed in submillimetre continuum emission than the lower J transitions. The aims of the spectral survey are to search for and categorize high-velocity outflows in order to identify protostars; to examine the column density in cores; to study the support mechanisms of protostars and their evolution; and to examine the turbulence and velocity structure of the parent molecular clouds (Ward-Thompson et al. 2007). SCUBA-2 continuum observations will also be made, and will cover an extremely large area compared to the current data sets available from e.g. SCUBA. As well as looking at the individual regions, the GBS will carry out statistical studies and comparisons on all the data sets and objects found.

1.2 The Serpens molecular cloud

The Serpens molecular cloud is a much-studied region of low-mass star formation, located ~ 230 pc from the Sun (Eiroa, Djupvik & Casali 2008, and references therein, in particular Straižys et al. 2003). It is forming a compact and high-density cluster of new stars, and its close proximity allows us to map its gas properties at high spatial resolution [a full width at half-maximum (FWHM) beam size of 3300 au at the distance of Serpens for ^{12}CO]. The cloud consists of two clusters of embedded Young Stellar Objects (YSOs) of which many possible Class 0/I/II sources have been detected by the *Spitzer* c2d survey using MIPS (Harvey et al. 2007b), and using both MIPS and IRAC (Harvey et al. 2007a). The region observed in this study is focused on the Serpens main cloud core, which contains the well-known submillimetre Class 0–I objects SMM

1–11 (Casali, Eiroa & Duncan 1993; Davis et al. 1999). Hogerheijde et al. (1999) presented high-resolution interferometric observations of some of these cores in a variety of molecular tracers. Evidence for infall towards SMM 2, 3 and 4 has been found (see e.g. Gregersen et al. 1997), further supporting the view that these are very young sources currently undergoing star formation. Duarte-Cabral et al. (2010) find evidence that the global structure of the cloud implies it consists of two colliding sub-clouds.

Much evidence of molecular outflows has been detected in the region in previous JCMT observations (White, Casali & Eiroa 1995; Davis et al. 1999). Hodapp (1999) measured the proper motions of H_2 jets in the north-west part of this region (in the vicinity of SMM 5, 9 and 10), further connecting these jets to outflow sources. The observations were centred on the region known as the Serpens cloud core, containing many protostars, dust sources, Herbig Haro (HH) objects and potential outflows. Eiroa et al. (2008) presented a recent review of the entire Serpens region. This paper presents new observations and results of outflow kinematics along with the general cloud properties.

2 OBSERVATIONS

Observations of the Serpens molecular cloud in the $J = 3 \rightarrow 2$ CO rotational transition were obtained using HARP at the JCMT. ^{12}CO observations were obtained in 2007 April and July, while ^{13}CO and C^{18}O observations were obtained simultaneously in 2007 August.

The telescope’s main beam efficiency η_{MB} is 0.63, taken from Buckle et al. (2009), where it was calculated from observations of planets. Each map was taken in ‘raster-scan’ mode. The telescope continually scans rows back and forth across the science region, writing out the data every 7.27 arcsec. The telescope regularly observes a reference position to correct for the atmospheric distortion. In order to minimize the variation of the noise across the map half the observations scan along the longer axis of the rectangular area being observed, and half along the shorter axis. The JCMT beam size at 345.796 GHz (^{12}CO $J = 3 \rightarrow 2$) is 14.6 arcsec, at 330.588 GHz (^{13}CO) it is 15.2 arcsec and at 329.331 GHz (C^{18}O) it is 15.3 arcsec.

In total, 3.5 h was spent observing the ^{12}CO and 6 h observing the ^{13}CO and C^{18}O . The observations were taken with a channel width of 0.42 km s^{-1} for ^{12}CO and 0.06 km s^{-1} for ^{13}CO and C^{18}O . These were resampled on to 1 km s^{-1} for the ^{12}CO and 0.1 km s^{-1} for the ^{13}CO and C^{18}O . The achieved noise levels on an unsmoothed, nearest-neighbour-gridded map were 0.10 K in 1 km s^{-1} for ^{12}CO and 0.93 and 0.88 K in 0.1 km s^{-1} channels for C^{18}O and ^{13}CO , respectively. The ^{12}CO has significantly exceeded the survey target rms level, which is 0.3 K in 1.0 km s^{-1} channels. However, the ^{13}CO and C^{18}O noise levels are significantly higher than the survey target rms (0.88 and 0.93 K compared with a target of 0.3 K in 0.1 km s^{-1}) therefore more observations are ongoing on this region to reduce the co-added noise to the required level. This will allow more detailed follow up work on the core kinematics; however, the current noise level is more than adequate to study the bulk gas conditions and energetics across the entire region.

One of the requirements of the GBS is to achieve reasonable rms uniformity across the scans. As a multi-detector array, HARP naturally has some variation in system temperatures for each detector,

¹<http://www.jach.hawaii.edu/JCMT/surveys/gb/>

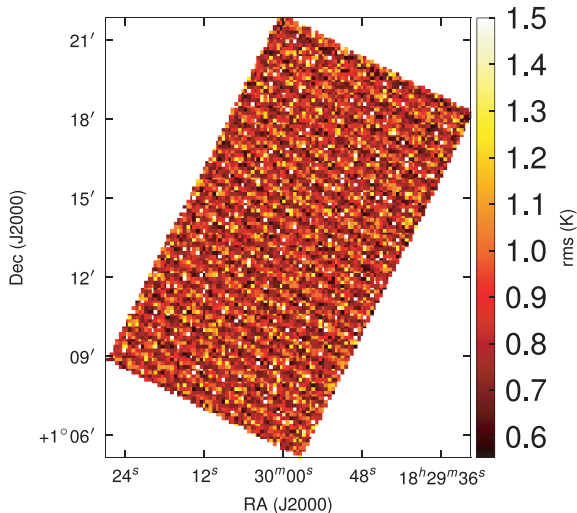


Figure 1. The noise on the ^{13}CO map: the root mean square integration of a line-free region from a nearest-neighbour gridded map with 7.27 arcsec pixels and 1 km s^{-1} channels.

and additionally during the survey science verification phase (in which these data were taken) not all detectors in the 4×4 array could be used, therefore completely even noise was not achieved. We illustrate the uniformity of the noise achieved in Fig. 1, which shows the rms values across the ^{13}CO map. As can be seen, the variation is low and although a grid pattern can be seen, it is constant across the map.

After the data were taken, the scans were analysed and for each scan the detectors showing anomalous baseline structure or excessive noise were removed from the reduction. The remaining data had a first-order baseline fitted to line-free regions of the spectra. This baseline was removed and the data were co-added, using nearest-neighbour gridding. The rest of the images shown here and used for analysis are gridded on to 3 arcsec pixels. The ^{12}CO data from each detector were re-scaled to correct for striping caused by varying detector responses (see Curtis, Richer & Buckle 2010, for the technique). A Gaussian kernel (using a FWHM of 9 arcsec) was used to grid these cleaned raw files into position–position–velocity cubes for each isotopologue (giving an effective beam size on the maps of 17 arcsec). The C^{18}O and ^{13}CO data files were gridded into separate files for each scan using a 10 arcsec FWHM Gaussian kernel; then the resulting files were mosaicked together using an 8 arcsec FWHM Gaussian kernel (giving an effective beamsize for the maps of 20 arcsec). This larger effective beamsize was used in order to increase the signal-to-noise ratio of the maps. In the ^{12}CO reduced cube, there was an anomalous baseline feature present in channels from 35.8 to 44.8 km s^{-1} . The shape was similar to other known instrumental effects in HARP/ACSIS data at the time the data were taken. The affected velocity region was blanked out, and then these channels were interpolated from surrounding data. Across most of the map, there is no emission at these affected velocities, with only a small region containing the tail of a high-velocity outflow having visible emission. The structure of the high-velocity tail affected in these spectra appears to be well matched by the simple interpolation.

The resulting noise measurement for the Gaussian smoothed maps used in the scientific analysis is 0.017 K for the ^{12}CO in 1 km s^{-1} channels, and 0.19 K for both the ^{13}CO and C^{18}O , respectively, in 0.1 km s^{-1} channels.

2.1 ^{12}CO map

The $J = 3 \rightarrow 2$ transition of the CO isotopologues observed here has critical densities of the order of 10^{4-5} cm^{-3} . Tracing these high densities allows us to look at the dense gas more intimately involved with the ongoing star formation than lower transitions, tracing lower densities, allow. It also allows us to examine the higher temperature emission from molecular outflows, as these transitions occur at a correspondingly higher energy level – 31 to 33 K – than the lower transitions.

Fig. 2(a) shows the integrated ^{12}CO emission; Fig. 3 overlays IR sources, submillimetre continuum sources and HH objects. As is evident from the integrated emission alone, the region is a complex, clustered star-forming region. The ‘finger-like’ extensions so common to CO observations in many regions are clearly discernible; however, it should be noted that these do not always correspond to obvious spatially compact bipolar outflows.

Our ^{12}CO $J = 3 \rightarrow 2$ map covers a region of 260 arcmin² centred on RA: $18^{\text{h}}29^{\text{m}}45^{\text{s}}$ Dec: $1^{\circ}13'57''$ (J2000). The region was extended westwards to follow the strong bow-shock that culminates in the HH object HH 106. This extended section has higher noise and was not followed up in ^{13}CO and C^{18}O . The integrated intensity map in Fig. 3 is not dominated by emission at the systemic velocity of the cloud, presumably at least in part due to the strong self-absorption present in the ^{12}CO spectra. Fig. 4 presents the spectra for all three isotopologues plotted on the same axes for each of the SMM cores, and Fig. 5 shows spectra from some typical positions throughout the cloud. Many of the ^{12}CO spectra exhibit either a double-peaked profile or a distorted Gaussian shape. By comparing the peak intensity and shape of the C^{18}O spectra from the same position as the ^{12}CO , it is clear that the shapes of the ^{12}CO line profiles appear to be caused by self-absorption rather than multiple velocity components.

The ^{12}CO emission is, therefore, dominated by the less dense blueshifted and redshifted high-velocity gas of the cloud. The absorption maximum appears slightly redshifted with respect to the local rest velocity – perhaps indicative of global infall in the cloud, as one would expect in a star-forming region. There are also prominent velocity wings present in the ^{12}CO spectra as can be seen in Fig. 4, also indicating the presence of molecular outflows in the region, some with velocities up to 20 km s^{-1} with respect to the local rest velocity. These outflows have been observed before with molecular tracers (White et al. 1995; Davis et al. 1999; McMullin et al. 2000; Olmi & Testi 2002) and with masers (Moscadelli et al. 2005); however the data presented here improve on the resolution of the previous single-dish CO studies. Recent *Spitzer* observations (Harvey et al. 2007a,b) have identified several deeply embedded sources within the Serpens molecular cloud – we would expect these sources to be of a Class 0 or early Class I nature, and thus drive powerful molecular outflows. Fig. 3 shows the integrated ^{12}CO emission, with the positions of YSO candidates, SCUBA cores and HH objects also displayed. We can see that the *Spitzer* deep sources align with the sources in the $850 \mu\text{m}$ SCUBA image, which are known in the literature as the 10 SMM sources, SMM 1–11, although note that there is no SMM 7. SMM 7 was first identified by White et al. (1995) at RA: $18^{\text{h}}29^{\text{m}}55.62^{\text{s}}$ Dec.: $+01^{\circ}14'52''$, but was not detected in the SCUBA map of Davis et al. (1999). There is not a clear C^{18}O emission peak present at its position in Fig. 2(d).

Fig. 6 shows the SCUBA $850 \mu\text{m}$ emission from Davis et al. (1999) with contours of red and blueshifted gas in ^{12}CO demonstrating that there are a large number of molecular

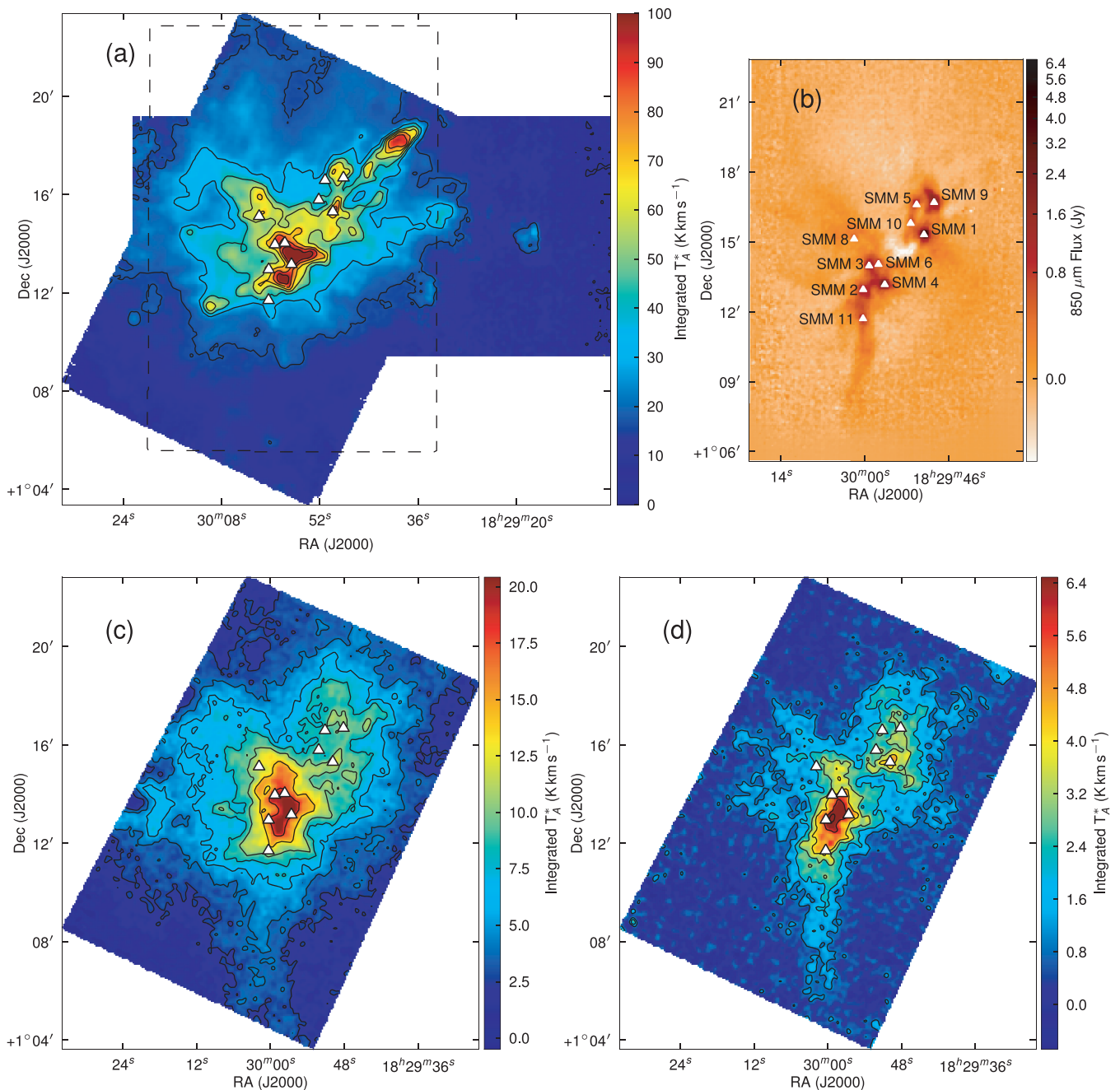


Figure 2. Presentation of the CO-integrated intensity images. For comparison the SCUBA data from Davis et al. (1999) are shown in (b). The C^{18}O image qualitatively follows the SCUBA emission. (a) Integrated ^{12}CO T_A^* emission in K km s^{-1} . Integrated from -1.12 to 15.88 km s^{-1} . The region observed with SCUBA is outlined in grey. (b) SCUBA 850 μm emission (Davis et al. 1999). Positions of the known submillimetre cores are shown and labelled. (c) Integrated ^{13}CO T_A^* emission in K km s^{-1} . Integrated from 4.54 to 10.44 km s^{-1} . (d) Integrated C^{18}O T_A^* emission in K km s^{-1} . Integrated from 5.55 to 9.95 km s^{-1} .

outflows associated with the Serpens sources. These maps are at a higher resolution than previous ^{12}CO studies, allowing more accurate flow and source identification, compared to the previous results of Davis et al. (1999), where some of the flows are unresolved. Fig. 7 shows another view of the ^{12}CO velocity structure of the cloud. In this three-colour image showing the red-shifted, blue-shifted and ambient emission (green) the strong red and blue lobes can be clearly seen.

2.2 ^{13}CO and C^{18}O maps

The isotopologues ^{13}CO and C^{18}O are much less abundant than ^{12}CO , with the abundance ratio for the ‘local’² interstellar medium (ISM) being calculated as $X^{12}\text{CO}/X^{13}\text{CO} = 77$ (Wilson & Rood

² Measured in the Orion GMC.

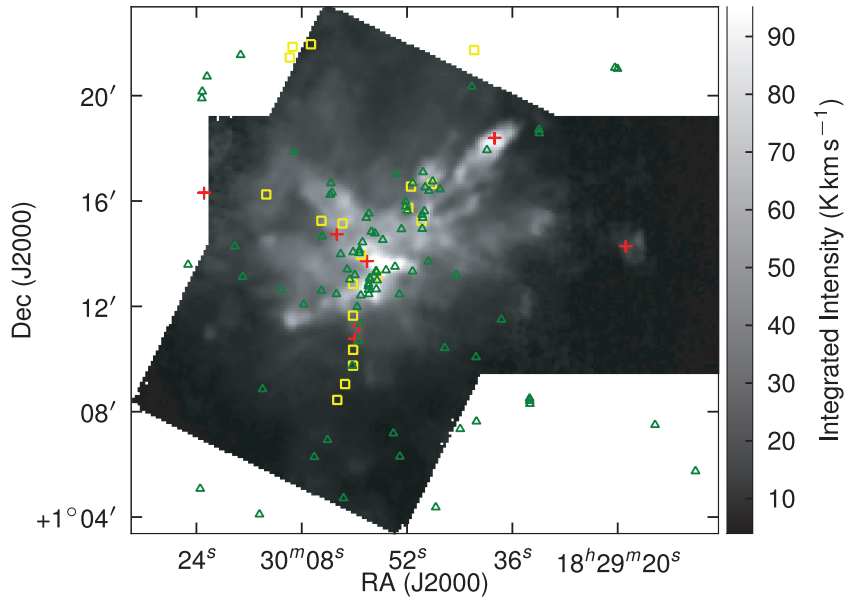


Figure 3. Integrated ^{12}CO emission, with SCUBA cores (Di Francesco et al. 2008) shown as yellow squares, c2d *Spitzer* YSO candidates (Evans et al. 2009) shown as green triangles and HH objects shown as red crosses (Davis et al. 1999). The $850\ \mu\text{m}$ SCUBA emission from Davis et al. (1999) is shown in contours.

1994). Being less abundant, these species are only seen on the denser parts of the sub-clusters, allowing us to probe the motions of the gas more closely associated with the protostars rather than the outflowing gas. Our ^{13}CO and C^{18}O maps (Fig. 2) cover a region of 17×11 arcmin centred on RA $18^{\text{h}}29^{\text{m}}58^{\text{s}}$, Dec. $1^{\circ}13'02''$ (J2000). Fig. 8 shows the SCUBA $850\ \mu\text{m}$ emission and overlays contours of the C^{18}O integrated intensity emission. We can see the C^{18}O emission traces the general shape of the dust and the filaments to the east and south identified by Davis et al. (1999) very clearly, although specific peaks do not align exactly with the position of the SCUBA cores. The C^{18}O spectra (in Fig. 4) show some evidence of multiple components along the line of sight (l.o.s). This suggestion is strengthened by the analysis of Duarte-Cabral et al. (2010), who suggest that there are multiple velocity components and that the whole cloud can be modelled as two colliding flows or sub-clouds. These multiple velocity components from the C^{18}O emission should not be confused with the double-peaked structure of much of the ^{12}CO emission. The double peaks occur at very different velocity scales than the C^{18}O multiple components, hence we believe the double peaks are due to self-absorption of the line by nearer, cooler gas.

The correlation between the C^{18}O and the continuum emission suggests that the C^{18}O emission is not optically thick in the bulk of the emission. This is also consistent with the CO spectra shown in Fig. 4 where the ^{13}CO still shows some self-absorption from colder redshifted gas as seen in the ^{12}CO spectra, whereas the C^{18}O spectra do not show such a clear pattern – although the presence of multiple components does make this less clear. In Section 3.1, we investigate the opacities of the isotopologues across the cloud.

It can be seen from these observations (see Fig. 2) that the ^{12}CO and C^{18}O emission is tracing different gas structures – the C^{18}O emission looks very similar to the SCUBA emission, tracing a clumpy medium containing dense cores. The ^{12}CO emission on the other hand is bright throughout the cloud, but is dominated by lobe-like filaments extending out from the cloud rather than clumpy emission in the centre of the cloud. The ^{12}CO does not appear to be tracing the SMM cores. This suggests that the ^{12}CO emission probably becomes optically thick in the gas surrounding the cores, and does not see all the way to the central infrared dense cores.

In order to look further at the different structures traced by the three isotopologues, Fig. 9 shows position–velocity (PV) diagrams taken along a line of constant declination through the position of SMM 1 in all three isotopologues. In this figure the PV diagrams of both ^{13}CO and ^{12}CO show evidence of self-absorption dips in the centre of the line, which are not seen in the C^{18}O . The ^{12}CO emission also clearly shows strong evidence for red- and blueshifted emission in the line wings, which is not clearly seen in the ^{13}CO and entirely absent in the C^{18}O maps. Again, this emphasizes that the isotopologues are truly tracing different environments, and specifically that the C^{18}O emission is not influenced by the molecular outflows, at least at the sensitivities of these data.

3 CLOUD CONDITIONS

3.1 Optical depth

The variation of optical depth across the cloud can be examined by looking at the ratio of intensities of the different isotopologues, $I_{^{13}\text{CO}}/I_{\text{C}^{18}\text{O}}$ and $I_{^{12}\text{CO}}/I_{^{13}\text{CO}}$, across the entire region being studied. The relation between the line intensity ratio and the optical depth (e.g. Rohlfs & Wilson 2000) at a specific velocity is

$$\frac{T_{^{12}\text{CO}}}{T_{^{13}\text{CO}}} = \frac{1 - \exp(-\tau_{12})}{1 - \exp(-\tau_{13})}, \quad (1)$$

where T is the brightness temperature and τ is the optical depth.

Ratio maps were created, displaying the ratio of the peak intensities of the isotopologues, thresholded at a 5σ peak value. For optically thin emission, the ratio of the intensities of two lines is expected to tend towards the relative abundances of these species as we look towards the edge of the map.

For the $^{12}\text{CO}/^{13}\text{CO}$ ratio, we see maximum values of only 10 or so at the most, compared with a measured abundance ratio of 77 (Wilson & Rood 1994), although this was from a different cloud. This implies that the ^{12}CO is optically thick through the whole of the cloud. Due to the extremely strong self-absorption in the ^{12}CO we do not attempt to calculate a valid optical depth from this ratio.

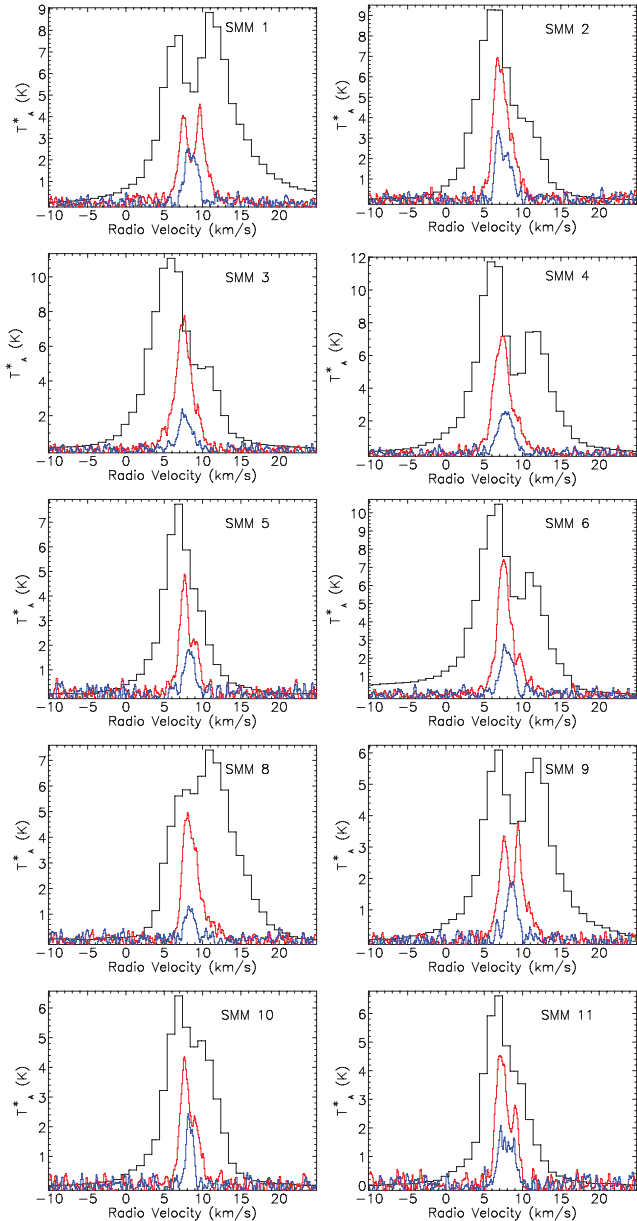


Figure 4. Spectra from the 10 SMM positions shown in Fig. 2. All three isotopologues are shown on the same axes. ^{12}CO is the highest intensity spectra (black), and C^{18}O is the weakest (blue). ^{13}CO is shown in red.

The optical depth in the cloud for C^{18}O and ^{13}CO can then be calculated by utilizing equation (1) above and the approximations that $\tau_{13} = X_{1318}\tau_{18}$ and $\tau_{12} = X_{1213}\tau_{13}$, where X is the appropriate abundance ratio. Often, this is calculated at the velocity of the peak channel. However, as we can see in the spectra from these cubes (see Fig. 4), there is visible self-absorption in the ^{13}CO and the ^{12}CO which would tend to limit the validity of this approach by underestimating the ratio by a varying amount across the map. Therefore, we follow the method in Ladd, Fuller & Deane (1998) and examine the ratio of the integrated intensities instead. Although the self-absorption will still cause the integrated ^{13}CO intensity to be underestimated, this should be a lower fractional error than would occur if the intensity ratio at the velocity of the peak was used. This remaining systematic underestimation will however boost the C^{18}O

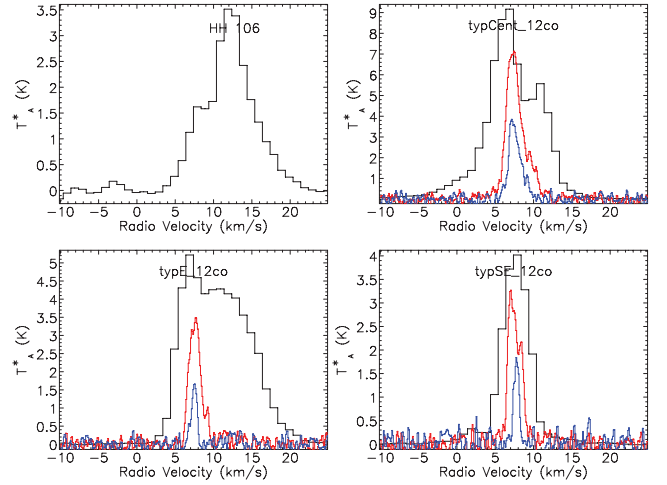


Figure 5. Spectra from HH 106 (^{12}CO only) and three typical non-core positions in the cloud. These were located at: 18:29:58.4 +1:13:21 (top right), 18:30:05.4 +1:16:30 (bottom left) and 18:30:03.4 +1:10:51.0 (bottom right). Colours as for Fig. 4

optical depth, particularly in the central regions where the ^{13}CO self-absorption is the strongest.

Fig. 10 shows the ratio map for the $^{13}\text{CO}/\text{C}^{18}\text{O}$ integrated ratio.

We then use

$$\frac{\int_{-\infty}^{\infty} T_{13}(\nu) d\nu}{\int_{-\infty}^{\infty} T_{18}(\nu) d\nu} = \frac{\int_{-\infty}^{\infty} 1 - \exp[-\tau_{13}(\nu)] d\nu}{\int_{-\infty}^{\infty} 1 - \exp[-\tau_{13}(\nu)/f] d\nu}, \quad (2)$$

where $\tau_{13}(\nu) = \tau_{13} \exp[-\nu^2/2\sigma^2]$, and $\tau_{18}(\nu) = \tau_{13}(\nu)/f$, to calculate the optical depth by numerically minimizing the following function:

$$\left| \frac{\int_{-\infty}^{\infty} 1 - \exp[-\tau_{13} \exp[-\nu^2/2\sigma^2]] d\nu}{\int_{-\infty}^{\infty} 1 - \exp[-\tau_{13} \exp[-\nu^2/2\sigma^2]/f] d\nu} - \frac{\int_0^{15 \text{ kms}} T_{13}(\nu) d\nu}{\int_0^{15 \text{ kms}} T_{18}(\nu) d\nu} \right|. \quad (3)$$

This method is very stable to the value of σ that is chosen; therefore we have simply used an average linewidth instead of estimating the Gaussian linewidth for each spectra. We used σ value corresponding to a linewidth of 1.5 km s^{-1} , the FWHM of an averaged C^{18}O spectra. The abundance ratio can be calculated for optically thin lines by looking at the intensity ratio towards the edge of the cloud. We see values approaching the canonical value of 8 (Frerking, Langer & Wilson 1982), therefore we feel confident both in using this as the abundance ratio for $^{13}\text{CO}/\text{C}^{18}\text{O}$ and that the C^{18}O emission really is optically thin across the cloud.

Across the map the $^{13}\text{CO}/\text{C}^{18}\text{O}$ ratio varies from around 3 to 8 across the central region to values from 2.6 to 7.0 towards the cores, with most clustered around a value of 3. This gives τ_{18} values of 0.07 to 0.9 towards the cores, and τ_{13} values of 0.61 to 7.3. This suggests that the C^{18}O 3–2 emission is optically thin across the map, and is even (marginally) optically thin towards the position of the submillimetre cores, and that the ^{13}CO 3–2 emission is transitional between optically thick and thin across much of the cloud, and optically thick towards the dense cores. Fig. 11 shows the C^{18}O optical depth calculated across the map. It is very noticeable that the regions of high optical depth do not correspond to the positions of the submillimetre SMM cores. This is not unexpected, as the peaks of the C^{18}O emission do not align exactly with that of the continuum cores. However, the effect of the C^{18}O ceasing to be optically thin towards extremely dense regions, as well as the possibility of depletion towards the centre of dense cores and the

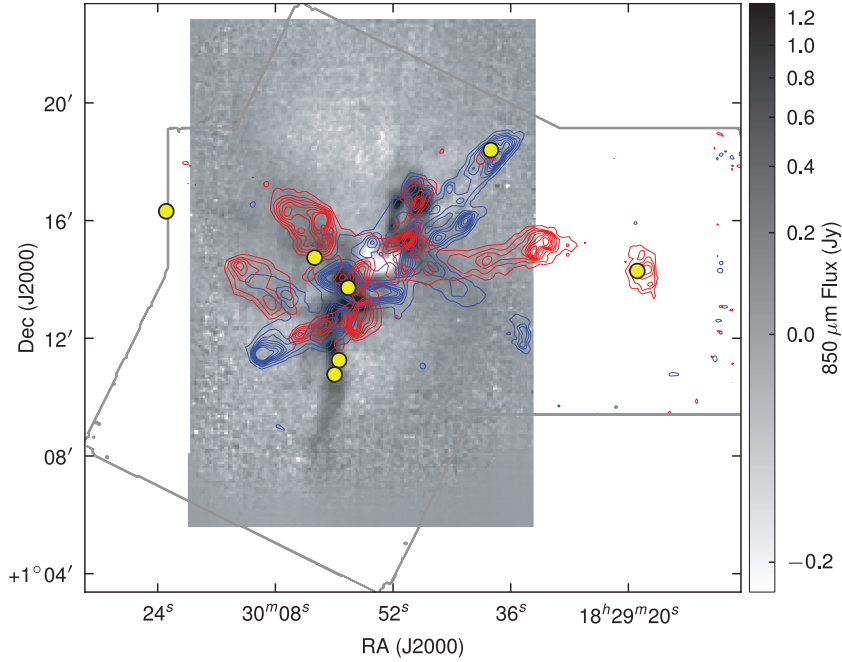


Figure 6. Grey-scale image is the SCUBA 850 μm emission from Davis et al. (1999). The blue contours represent blueshifted ^{12}CO gas and red contours represent redshifted ^{12}CO gas. The contour levels go up in 2.5 K km s^{-1} steps, starting from 2.5 K km s^{-1} . The integration ranges are -4 to 4 km s^{-1} for blueshifted gas and 14 to 22 km s^{-1} for the redshifted gas. The positions of known HH objects (from Davis et al. 1999) are shown as circles (see Fig. 19 for labelling).

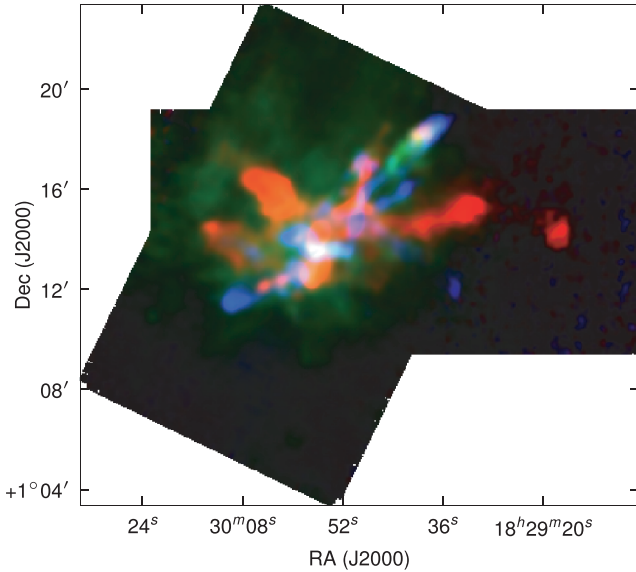


Figure 7. Red–green–blue image of integrated intensity structure in ^{12}CO . Red: 11.8 – 57.8 km s^{-1} . Green: 4.8 – 10.8 km s^{-1} . Blue: -42.2 – 3.8 km s^{-1} .

slight self-absorption present in the ^{13}CO emission prevent us from investigating this further.

3.2 Excitation temperature

The excitation temperature of the molecular gas can be calculated from the peak temperature of emission from optically thick gas (via the assumption of local thermodynamic equilibrium). In our observations, however, the most optically thick tracer – ^{12}CO – is

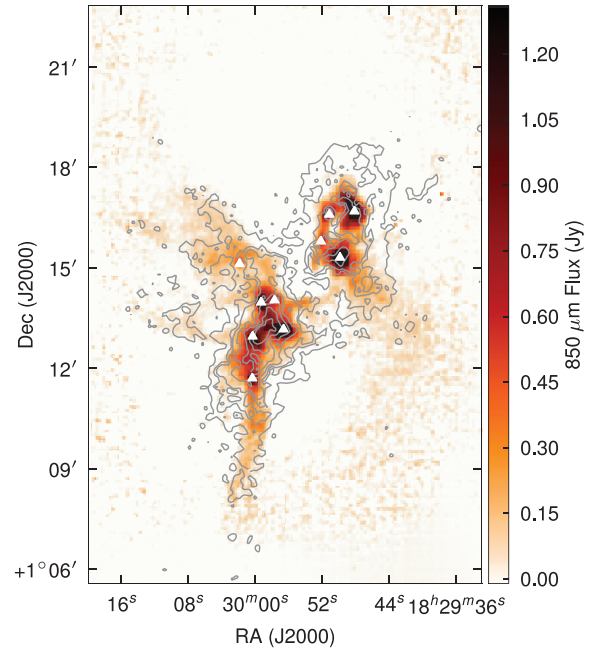


Figure 8. SCUBA 850 μm emission from Davis et al. (1999) with C^{18}O integrated intensity contours overlaid. Contour levels are at 1 – 7 K km s^{-1} in 1 K km s^{-1} steps, and the integration was from 5.3 to 10.6 km s^{-1} .

complicated by the strong self-absorption features seen in the ^{12}CO line profiles across much of the cloud. This would underestimate the excitation temperature in these dense regions. However, as we have calculated that the ^{13}CO emission is just optically thick across much of the cloud, we can also calculate the excitation temperature

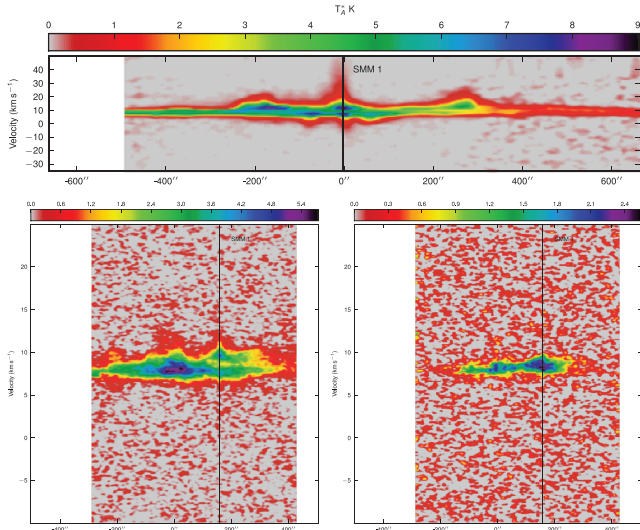


Figure 9. PV cuts through the position of SMM 1 along a line of constant declination, in all three isotopologues. The ^{12}CO map is on the top, then the ^{13}CO is below on the left and the C^{18}O on the right. The black lines indicate the position of SMM 1.

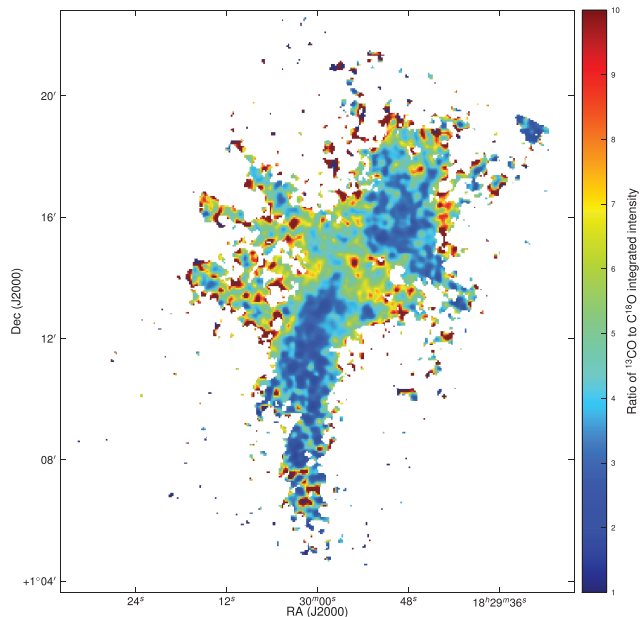


Figure 10. Ratio of integrated intensity of ^{13}CO over C^{18}O both maps integrated from 0 to 15 km s^{-1} .

from this emission, using

$$T_{\text{B}} = T_0 \left(\frac{1}{e^{T_0/T_{\text{ex}}} - 1} - \frac{1}{e^{T_0/T_{\text{bg}}} - 1} \right) (1 - e^{-\tau_{\nu}}) \quad (4)$$

where T_{B} , the main beam temperature, is assumed to be the same as the peak temperature of the transition, T_0 is $h\nu/k_{\text{B}} = 16.6\text{ K}$ for ^{12}CO and 15.9 K for ^{13}CO , and $T_{\text{bg}} = 2.73\text{ K}$ is the temperature of the cosmic background. τ is the optical depth for the transition of interest and is assumed to be infinity here. This equation assumes that the emission completely fills the beam. This gives

$$T_{\text{ex}}(^{12}\text{CO}) = \frac{16.6\text{ K}}{\ln \frac{16.6\text{ K}}{T_{\text{peak}} + 0.0377\text{ K}} + 1} \quad (5)$$

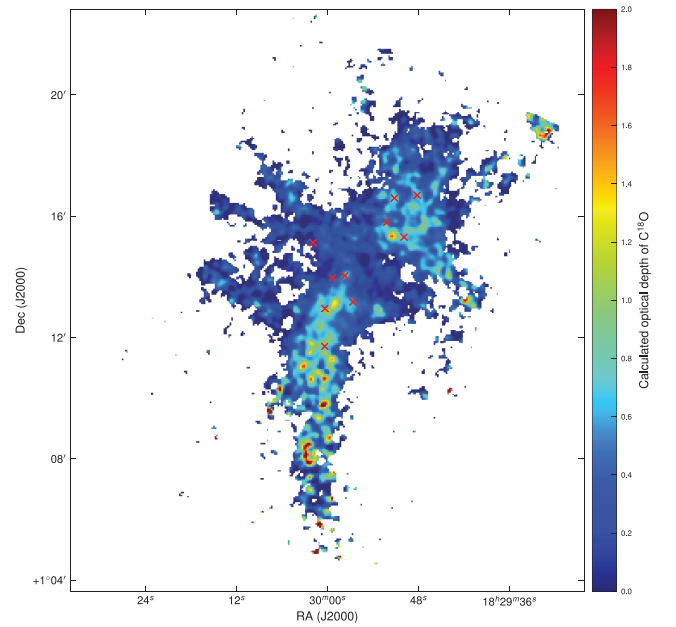


Figure 11. Calculated τ_{18} across the map.

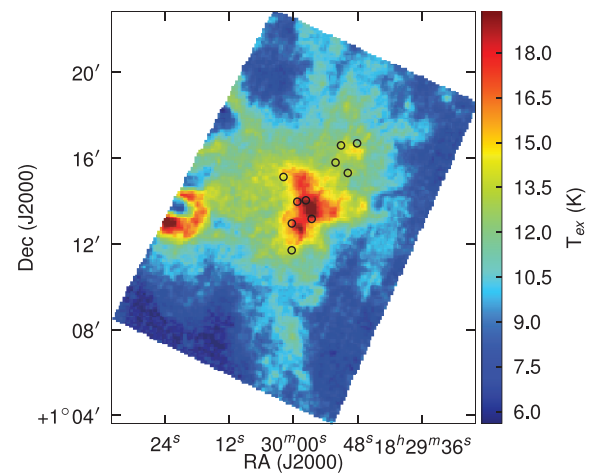


Figure 12. Excitation temperature from ^{13}CO emission in K. Positions of the submillimetre cores are shown as circles (i.e. SMM 1–11) from Davis et al. (1999). This was calculated assuming high optical depth.

$$T_{\text{ex}}(^{13}\text{CO}) = \frac{15.9\text{ K}}{\ln \frac{15.9\text{ K}}{T_{\text{peak}} + 0.0472\text{ K}} + 1} \quad (6)$$

The results for both ^{13}CO and ^{12}CO are shown in Figs 12 and 13. ^{12}CO gives us a mean excitation temperature of 17 K across the map, and temperatures towards the positions of the cores of $21\text{--}33\text{ K}$. These positions will, however, be looking at the excited gas from molecular outflows instead of the cores themselves. These temperatures may be underestimated as the ^{12}CO emission is strongly self-absorbed towards the bulk of the cloud. However, by contrast the excitation temperature calculated from the ^{13}CO emission is significantly lower – a mean temperature across the cloud of 13 K , and temperatures towards the cores ranging from $16\text{ to }22\text{ K}$. This ^{13}CO temperatures have been calculated assuming high optical depth. Although we have calculated the ^{13}CO opacities towards the centre of the map (where they are highest), we do not have ^{13}CO opacities for

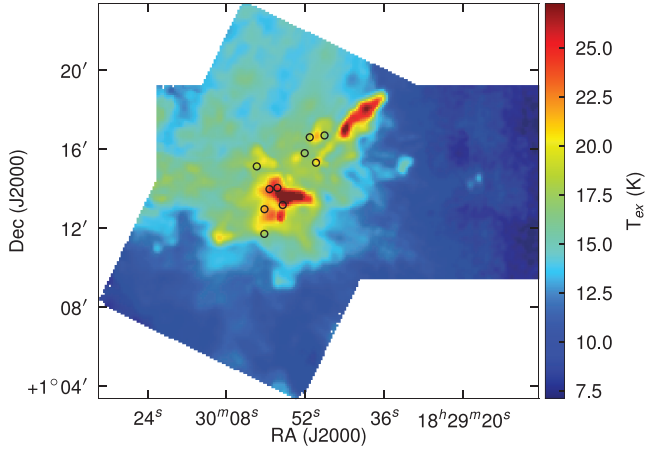


Figure 13. Excitation temperature from ^{12}CO emission in K. Positions of the submillimetre cores are shown as circles (i.e. SMM 1–11) from Davis et al. (1999).

those regions towards the edges of the map where the C^{18}O emission is weak or not detected. Therefore, we have not been able to correct for the ^{13}CO opacity in these regions, but we expect that the assumption of high optical depth will be least valid in these areas. Caution must be used when drawing conclusions from the excitation temperatures in these regions.

The difference in temperatures derived from the ^{13}CO and ^{12}CO maps is interesting, particularly given that we expect the ^{12}CO temperature to be significantly underestimated due to the stronger self-absorption. Fig. 13 suggests that the excitation temperature estimated from the ^{12}CO appears to trace some of the outflow structure in this cloud. This can be most clearly seen in the hot lobe-like structure visible in the NW of Fig. 13. This structure corresponds to the position of HH 460, and there is known bright H_2 emission in the region. This suggests that shocks are primarily responsible for producing the higher ^{12}CO temperatures.

Also noticeable in this analysis is an arc of high temperatures towards the east of the ^{13}CO map in Fig. 12. Near to this position there are both a reflection nebula and the B-type star HIP 90707. It is possible that these are influencing the gas temperatures in this region. The ^{13}CO map shows narrow but bright spectral line profiles in this region.

3.3 Cloud mass

The mass of the cloud has been estimated from the integrated C^{18}O intensity. This calculation assumes that the C^{18}O emission is optically thin. This is generally expected to be true everywhere in molecular clouds apart from the centre of the very densest cores, and for Serpens this was confirmed above in Section 3.1. These extremely dense regions contain only an insignificant proportion of the total mass in this region. The ratio of C^{18}O to H_2 is taken to be 10^{-7} , and the distance to the cloud was assumed to be 230 pc (Eiroa et al. 2008). T_{ex} , the excitation temperature, was assumed to be 12 K. This seems reasonable both as a fairly standard value for cold gas in molecular clouds and from the excitation calculations given above from the ^{12}CO and ^{13}CO emission.

$$M_{\text{C}^{18}\text{O}} = 4.0 \times 9.34 \times 10^{-4} \left(\frac{\text{Pixel size}}{3.6 \times 10^{-3} \text{ pc}} \right)^2 \times \left(\frac{\eta_{\text{MB}}}{0.63} \right)^{-1} \int T_A^*(\nu) M_{\odot}. \quad (7)$$

This gives a mass for the cloud of $203 M_{\odot}$. Quantifying the error on this number is not trivial given the large number of uncertainties in the input parameters and assumptions; however, the largest sources of systematic errors are probably contained in the estimate of the abundance and in the assumption of local thermodynamic equilibrium (LTE). The relative abundance of CO to H_2 has not been measured in Serpens, therefore we have adopted the standard literature value.

An estimate of the virial mass of the cloud can be calculated assuming a spherical cloud of uniform density via (Rohlf & Wilson 2000)

$$M_{\text{virial}} = 250 \left(\frac{v_{\text{fwhm}}}{\text{km s}^{-1}} \right)^2 \left(\frac{R}{\text{pc}} \right) \quad (8)$$

where v_{fwhm} is the FWHM 1D velocity in km s^{-1} and R is the radius of the cloud in pc. From the C^{18}O emission, we see a full-width half-max line of between 1 and 2 km s^{-1} ; therefore we take a value of v_{fwhm} of 1.5 km s^{-1} . The bright C^{18}O emission in the cloud is roughly 12 arcmin long and approximately 6 arcmin wide at the widest region, so we assume a diameter of 9 arcmin and therefore a radius of 4.5 arcmin, which corresponds to 0.3 at 230 pc. This gives a virial mass of $169 M_{\odot}$.

This virial mass is approximately 80 per cent of the measured C^{18}O mass, suggesting that the cloud is in a bound state. However, this result is of course subject to the same sort of systematic uncertainties as the mass estimate. These large uncertainties prevent us from drawing a more firm or quantitative conclusion about the state of the cloud other than to estimate that the measured C^{18}O mass is close to the virial mass, even if we attempted to use a more complex model of the density.

3.4 Global energetics

We can compare the different energetics present in the cloud by making some simple approximations. We can estimate the gravitational binding energy and the turbulent kinetic energy using the following equations:

$$E_{\text{grav}} = -\frac{3GM^2}{5R} \quad (9)$$

$$E_{\text{kin}} = \frac{3}{2} M \sigma^2, \quad (10)$$

where G is the gravitational constant, M is the mass of the gas in the cloud, R is the estimated size of the cloud and σ is the estimated 1D velocity dispersion in the cloud, equal to $v_{\text{fwhm}}/2.35$. This assumes a uniform density cloud. A more centrally condensed cloud would be more tightly bound (i.e. would have a more negative gravitational binding energy). Similarly, due to the M^2 factor involved, the uncertainties in the mass of the cloud will produce a large uncertainty in the gravitational binding energy. The error in the assumption of a single velocity dispersion for the entire cloud will also produce large uncertainties in these values, due to the σ^2 factor.

The virial mass calculated above corresponds to a gravitational binding energy of $245 M_{\odot} \text{ km}^2 \text{ s}^{-2}$. The turbulent kinetic energy can be estimated by measuring the CO linewidth in regions where the emission is not affected by outflow activity, therefore we use the optically thin tracers. The ^{13}CO and C^{18}O maps give roughly similar results of ~ 1.5 – 2 km s^{-1} for the linewidth, 2 km s^{-1} is used here, giving a turbulent kinetic energy of $220 M_{\odot} \text{ km}^2 \text{ s}^{-2}$.

The energetics of the cloud are summarized in Table 1, along with the global outflow energy from Section 5.1.

Table 1. Summary of the energetics of the Serpens molecular cloud.

	Energy ($M_{\odot} \text{ km}^2 \text{ s}^{-2}$)
Gravitational binding	245
Turbulent kinetic	220
Global outflow kinetic energy	
Along l.o.s.	51
Assuming random inclination	153

This analysis suggests that the cloud is gravitationally bound. However, it is important to reiterate that there are large uncertainties in the estimates of the values presented here.

We can also examine the importance of the outflows in this region. The outflow momenta and energy have been derived by assuming that the measured speeds are along the l.o.s.; this will underestimate the values. To estimate the correction to this, we assume the direction of the outflows is distributed isotropically. As we have many flows contributing to the global outflow momentum and energetics, this is a good approximation. Table 1 shows the corrected values. These suggest that the outflow energy is approximately 70 per cent of the turbulent energy. This result would suggest that in this dense, clustered region the outflows are a very important effect and could be the dominant factor driving the local turbulence. However, it is important to note that there are significant uncertainties in the estimation of these variables (as mentioned in the discussion of the mass, and in further discussion in Section 5.1). Further work on disentangling the individual outflows and on analysing the detailed structure of the entire region will be required to quantify this more accurately, possibly using observations of other tracers.

4 VELOCITY STRUCTURE FROM $C^{18}O$

The $C^{18}O$ emission, which is not tracing outflows and is optically thin across the whole extent of the Serpens cloud, allows us to study the velocity structure of the cloud in detail, with no obvious contamination from infall and outflow motions at the sensitivity of these observations. In the following sections we will analyse the velocity structure using velocity-coded three-colour plots and PV diagrams through the region, to try to understand the general dynamics of the region.

4.1 Global velocity

The velocity structure of the dense gas of the Serpens cloud can be seen in Fig. 14 as a velocity-coded three-colour plot. A first glance at this figure shows that the blueshifted emission is east of the Serpens filament, whereas the red emission is mainly west of it. This gradient has been previously detected by other authors (Olmí & Testi 2002), who interpreted it as a global rotation of the cloud. However, this conclusion was limited by the resolution of their data, which could not resolve the velocity structure in as much detail as we can.

Fig. 14 demonstrates that this velocity structure is more complex than simple rotation, by showing a three-colour plot of the $C^{18}O$ redshifted, blueshifted and central-velocity emission. For instance, we can see, in the SE end of the Serpens filament (the SE sub-cluster) a sharp merger/overlap of the blue and the red emission, not expected in a solid body rotation scenario. On the other hand, the NW end of the filament (the NW sub-cluster) has very little blueshifted emission. This velocity structure was also suggested to be possibly a shear motion (Olmí & Testi 2002) or a collision of

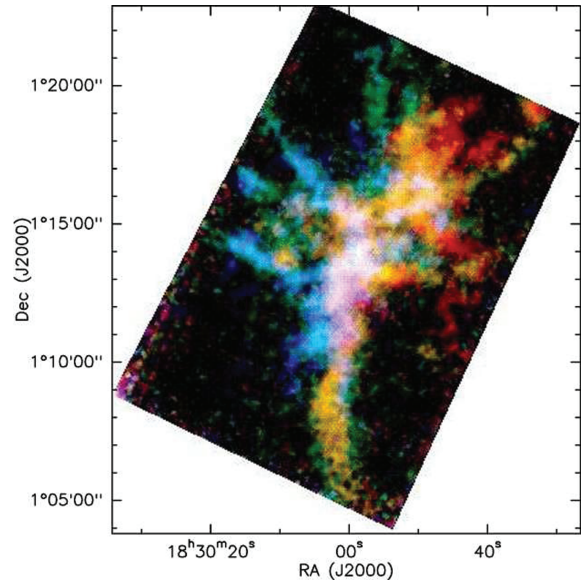


Figure 14. Velocity-coded three-colour plot of the $C^{18}O J = 3 \rightarrow 2$. Each colour represents the maximum value in the following velocity intervals: blue: $5\text{--}7.7 \text{ km s}^{-1}$; green: $7.7\text{--}8.3 \text{ km s}^{-1}$ and red: $8.3\text{--}11 \text{ km s}^{-1}$.

two clouds/flows where the interface coincides with the SE end of the filament (Duarte-Cabral et al. 2010).

Another noticeable feature visible in this view of the $C^{18}O$ velocity structure are the gas streams east of the filament. Note that these are not seen at the west, nor do they correlate with any of the outflows seen in ^{12}CO . These small filaments roughly perpendicular to the main filament are commonly seen in filamentary molecular clouds, but their origin is not yet clear (Myers 2009).

4.2 Position-velocity diagrams

In order to look at the velocity structure at specific positions we have created PV diagrams. By studying several PV diagrams from our $C^{18}O$ maps, we can get a better sense of how the velocity changes and evolves across the cloud. Our approach to such a study involves several cuts both with constant Declination and with constant RA. Fig. 15 shows the positions of the PV cuts used here.

Figs 16 and 17 show PV diagrams (horizontal slices of the data cube) at five fixed Declinations, varying the Right Ascension. Fig. 16 cuts through the NW sub-cluster, where we can note that this sub-cluster is represented by a velocity mainly between 8 and 8.5 km s^{-1} . However, there is some lower velocity gas weakly emitting east of the sub-cluster, with velocities around 7.5 km s^{-1} . Whether this gas is physically connected with the higher velocity gas is not clear, as it could either represent a separate cloud with a slightly different velocity, or the same cloud undergoing rotation. Therefore, we must examine the evolution of these components as we look southwards through the cloud in order to understand what these gas components are tracing.

Fig. 17 shows the velocity structure of the SE sub-cluster. Here, the two velocity components, which in the north are very well separated, begin to merge. As we move south the components become more offset from each other in velocity, and we see regions that are clearly reproduced by two velocities (one around 7 km s^{-1} and the other around 8.5 km s^{-1}). Note that the regions which also show dust emission are coincident with regions where the two velocities coexist along the l.o.s. Finally, the lower velocity gas ceases to exist,

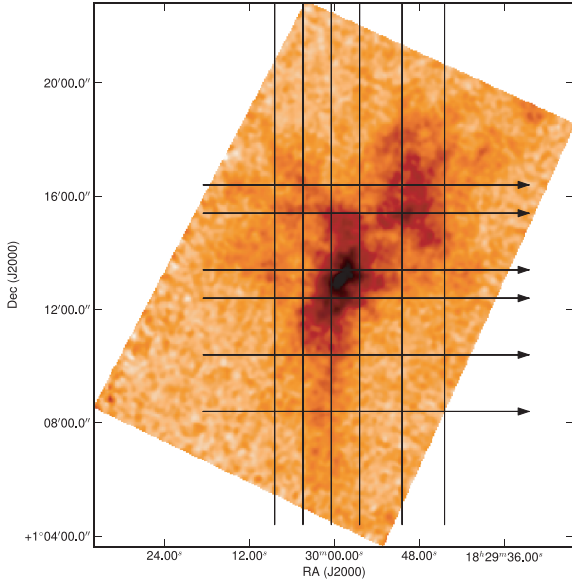


Figure 15. Integrated $C^{18}O$ map showing the positions of the PV diagrams used in this section.

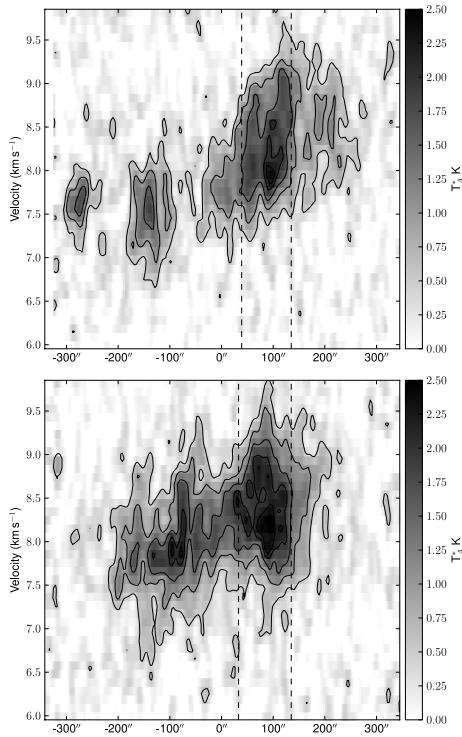


Figure 16. Horizontal PV diagrams in grey-scale and contours of the $C^{18}O$ $J = 3 \rightarrow 2$ emission. These represent the typical velocity structure in the NW sub-cluster. The diagrams are displayed with decreasing Declination, i.e. from north to south, and at constant Declinations of $1^{\circ}16'24''$ (top) and $1^{\circ}15'24''$ (bottom). Right Ascension varies from $18^{\text{h}}30^{\text{m}}18^{\text{s}}.5$ to $18^{\text{h}}29^{\text{m}}32^{\text{s}}.5$ (offset of +277 to -412 , respectively) on both diagrams. The dust emission seen in $850 \mu\text{m}$ lies between the dotted lines.

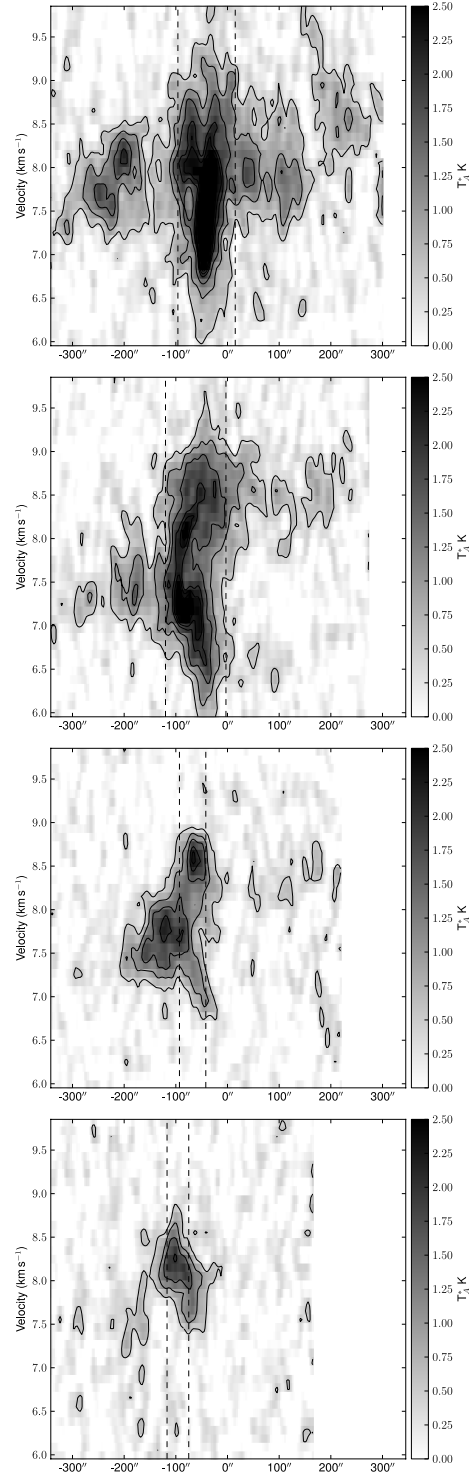


Figure 17. Horizontal PV diagrams in grey-scale and contours of the $C^{18}O$ $J = 3 \rightarrow 2$ emission. These represent the typical velocity structure in SE sub-clusters. The diagrams are at constant Declination (from top to bottom panel) of $1^{\circ}13'24''$, $1^{\circ}12'24''$, $1^{\circ}10'24''$ and $1^{\circ}08'24''$. Right Ascension varies from $18^{\text{h}}30^{\text{m}}18^{\text{s}}.5$ to $18^{\text{h}}29^{\text{m}}32^{\text{s}}.5$ (offset of +277 to -412 arcsec, respectively) on all the diagrams. The dust filament seen in $850 \mu\text{m}$ lies between RA offsets of -120 and -180 arcsec.

and at the very southern end of the filament solely consists of the higher velocity gas, at around 8.3 km s^{-1} .

We also study the velocity structure using vertical PV diagrams (constant RA) in Fig. 18. The information we get from here adds to the horizontal diagrams, in the sense that we can confirm the complex velocity structure, including the double velocity component towards the south sub-cluster (best seen in Fig. 18, top right panel). We can also see velocities below 8 km s^{-1} towards the northern region, in the first two panels. Because this corresponds to higher RA positions, these lower velocities in the north are only seen in regions offset to east from the sub-cluster seen in $850 \mu\text{m}$ emission. The two last panels of Fig. 18 (bottom row, centre and right panels) show the bulk of emission towards the NW sub-cluster, which traces well the $850 \mu\text{m}$ continuum emission, showing us the velocities all concentrated between 8 and 8.5 km s^{-1} . The outflow structure of the cloud is complex. Although there appear to be many outflows in this region, many are overlapping. Instead of attempting to assign spectra arbitrarily to one or another of an overlapping outflow in order to calculate their properties, we have decided to look first at the global outflow properties (i.e. energetics for all the high-velocity gas), and then to look individually at those outflows that can be spatially located via their very high velocity emission.

5 OUTFLOWS

5.1 Global outflow properties

To calculate the global outflow properties, we wish to look at all the gas that is moving at a significantly red- or blueshifted velocity from the line centre. However, it is not possible to completely exclude the ambient emission, and some proportion of this will also be included in these calculations.

We can calculate some basic kinematic properties for the global properties of the outflowing gas. Examination of the spectra in the cloud shows that ambient ^{12}CO spectra away from the outflows appear to cover a velocity range of 6 to 10 km s^{-1} . This is assumed to include ambient emission for the entire cloud and is excluded from the integration. Therefore, the integration ranges used are -15 to 6 km s^{-1} for the blueshifted emission and 10 to 30 km s^{-1} for the redshifted emission.

The masses were calculated under the assumption of LTE, a distance of 230 pc and assuming optically thin emission in the line wings with an excitation temperature of 50 K (White et al. 1995; Davis et al. 1999). Although this is higher than the peak excitation value we calculated earlier, it is expected that the gas in the outflows will be considerably warmer than that in the bulk of the gas.

$$M_{12\text{CO}} = 2.2 \times 10^{-6} \left(\frac{X_{\text{CO}}}{10^{-4}} \right)^{-1} \left(\frac{\eta_{\text{MB}}}{0.63} \right)^{-1} \left(\frac{A_{\text{pixel}}}{9 \text{ arcsec}^2} \right) \int T_A^*(v) dv M_{\odot}. \quad (11)$$

The momentum and energy are estimated similarly, by replacing $\int T_A^* dv$ by $\int T_A^* |v - v_0| dv$ and $0.5 \times \int T_A^* (v - v_0)^2 dv$, where v_0 is the central velocity. Here, an average central velocity value is used for the whole cloud.

The global results for the Serpens cloud are summarized in Table 2. In Table 1 we give the total energy from both global outflow values: $50 M_{\odot} \text{ km}^2 \text{ s}^{-2}$. It is of course again important to consider the sources of systematic uncertainty affecting these figures. Our assumption of the excitation temperature of 50 K , our chosen value for the CO abundance and our assumption of LTE are sources of uncertainty in these values. We also expect some proportion of the

Table 2. Global outflow properties, both along the l.o.s. only and corrected for a random distribution of inclinations (corr.).

	Mass (M_{\odot})	Momentum ($M_{\odot} \text{ km s}^{-1}$)	Energy ($M_{\odot} \text{ km}^2 \text{ s}^{-2}$)
I.o.s.			
Blue	1.3	6.1	28
Red	1.8	6.3	23
Corr.			
Blue	-	12.2	84
Red	-	12.6	69

shocked gas to be disassociated from its molecular form, and this will be a larger effect at the high velocities. We have also assumed that the entire line wing is optically thin; in fact this may well not be true, especially at the velocities close to the ambient cloud emission. This effect may mean that our values for the outflow masses are significantly underestimated. There may also be an effect on the momentum and energy estimated, but the optical depth is likely to be a less important factor and the disassociation a larger factor as these values are dominated by the high-velocity emission. These effects would tend to increase the values shown here. It is also important to reiterate that there will be some contamination of the values shown here by the ambient gas.

Equation (11) only provides us with the energy and momentum along the l.o.s., and we must correct for the inclination of the outflows if we wish to calculate 3D values. The outflow velocity should be corrected by $1/\cos(i)$ from the l.o.s. velocity, where i is the inclination angle. If we assume that the outflows are in an isotropic random distribution, this will increase the momentum by a factor of 2 and the kinetic energy by 3.

We have also made a rough estimate of the dynamical age of the outflows in the region. An estimate of the average flow lobe length was found from Fig. 6 of 210 arcsec (0.23 pc at $D = 230 \text{ pc}$) in the plane of the sky. The average maximum velocity in the l.o.s. is $\sim 14 \text{ km s}^{-1}$, thus obtaining a value of $1.6 \times 10^4 \text{ yr}$. This very young age agrees with the conclusions in the literature that the Serpens sources are Class 0/I YSOs (Casali et al. 1993; Testi & Sargent 1998). The values for these energetic properties correspond well to those found in Davis et al. (1999).

5.2 Effect of outflows on global energetics

The results in Tables 1 and 2 allow us to discuss the validity of the theory of supersonic turbulence sustained by molecular outflows.

If we apply a correction for random inclination, we estimate the total kinetic energy contained in the outflows to be of the order of 70 per cent of the total turbulent kinetic energy (see Section 3.4). This suggests that the outflows are a strong influence on the structure and energetics of the Serpens cloud core, and studies of this region must take care to account for them (particularly with respect to small-scale structure).

Our finding that the turbulent kinetic energy and the global outflow energy are of comparable size fits well with theories and simulations that involve the driving of supersonic turbulence by outflows in regions of active star formation (see e.g. Li & Nakamura 2006; Matzner 2007). However, it is still necessary to identify a mechanism that can convert the outflow momentum (directed outwards from the cloud) into the turbulent energy. An analytical model for this process was developed by Matzner (2007), who proposed that molecular cloud turbulence can be driven by collimated protostellar outflows, resulting in a cascade of momentum rather than energy.

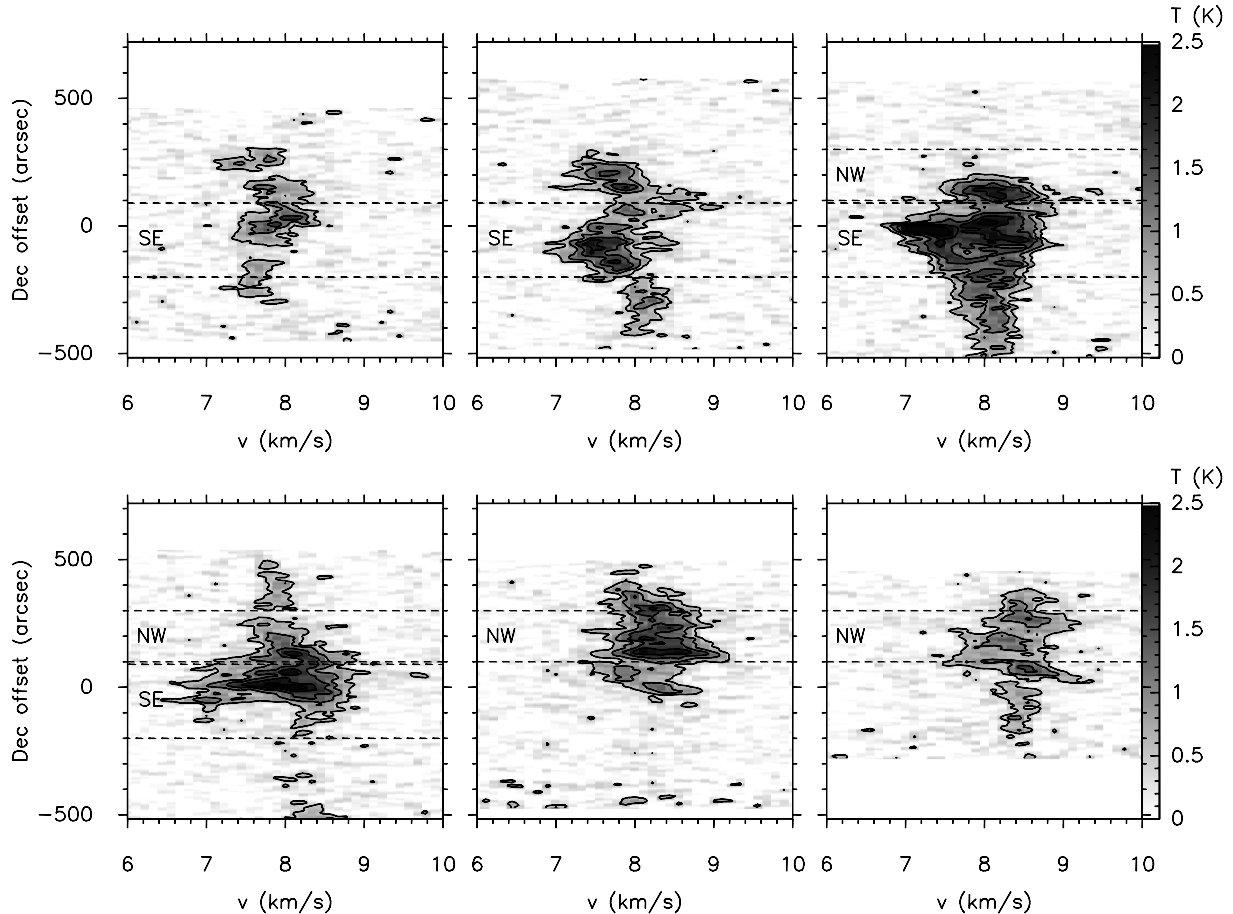


Figure 18. Vertical PV diagrams in grey-scale and contours representing the $\text{C}^{18}\text{O } J = 3 \rightarrow 2$. Declination ranging for $1^{\circ}4'24''.1$ to $1^{\circ}25'0''.8$ (offset from -515 to 720 arcsec, respectively) on all diagrams. The NW sub-cluster lies in Dec. offsets of $+90$ to $+270$ arcsec and the SE sub-cluster between -180 and $+90$ arcsec. Panels are displayed with decreasing Right Ascension (i.e. from east to west), with upper row being mostly representative of the SE sub-cluster whereas the lower row represents the NW sub-cluster. From top-left to lower-right diagrams, the cuts are at constant RA of $18^{\text{h}}30^{\text{m}}8^{\text{s}}.4$, $18^{\text{h}}30^{\text{m}}4^{\text{s}}.4$, $18^{\text{h}}30^{\text{m}}0^{\text{s}}.4$, $18^{\text{h}}29^{\text{m}}56^{\text{s}}.4$, $18^{\text{h}}29^{\text{m}}50^{\text{s}}.4$ and $18^{\text{h}}29^{\text{m}}44^{\text{s}}.4$.

Numerical simulations by Li & Nakamura (2006) and Carroll et al. (2009) appear to be consistent with this picture.

A further interesting comparison can be made between the turbulent kinetic energy and the gravitational binding energy. Since the binding energy is very similar to the turbulent kinetic energy this suggests that the entire cloud is only weakly bound and that some small, local, regions may well be in a state of collapse whereas others are in a state of expansion. This is one of the expected observations of the theory of star formation control by supersonic turbulence (see McKee & Ostriker 2007, and references therein, e.g. Mac Low & Klessen 2004). Further insight can be gained by considering the ratio of kinetic outflow energy to gravitational binding energy. A value of ~ 0.7 is indicative that outflows are extremely important to understand the cloud support mechanism. However, we expect the uncertainties in the estimation of the various parameters are large enough to prevent a more firm conclusion.

5.3 Individual outflows

As can be seen from the ^{12}CO channel maps presented in Fig. 19, the ^{12}CO high-velocity structure is extremely complex – identifying outflows from the ^{12}CO emission alone is extremely difficult. We see considerable ‘finger-like’ structures in this region that correspond to large-scale outflow structure across the cloud. Although

areas containing high-velocity red- and blueshifted gas can be seen clearly in the channel maps, categorizing these into neat bipolar lobes is not so simple. However, there are reasonable amounts of complementary data available. The presence of known HH objects is indicated in Fig. 6, and a comparison with the positions of known cores allows a few more clear-cut outflows to be identified. Figs 22 and 23 show PV diagrams along some of these outflows.

5.3.1 Features from the channel maps

Fig. 20 displays some of the clearer potential outflow structures from the channel maps, circled and labelled.

A: Examining the velocity structure from the ^{12}CO channel maps (Fig. 19) and the red- and blueshifted contours allows us to immediately see one strong feature – the long extended redshifted emission westwards from the centre of the map, leading to HH 106. There is no blueshifted emission obviously lining up with this large feature, but the examination of the spectra in this region clearly shows the strong redshifted line wing. The spectra also show that the maximum velocity of the emission increases along the flow as it heads away from the main cloud, reaching up to 25 km s^{-1} .

B: We also see a clump of emission towards the position of HH 106 in the extended region of the ^{12}CO map; the spectral line

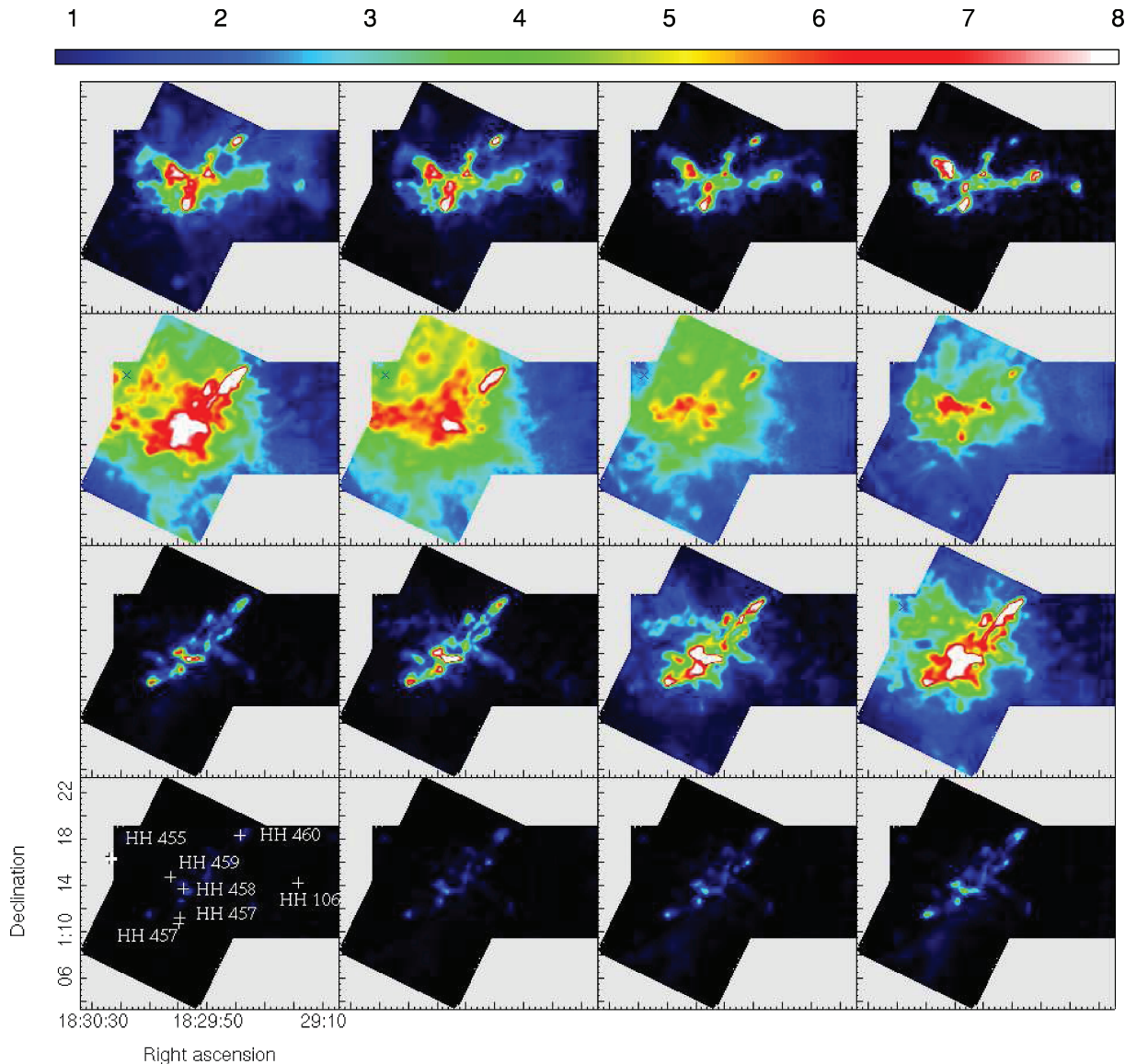


Figure 19. ^{12}CO channel maps of T_A^* . Beginning at -1.1 km s^{-1} in lower left and increasing up to 14.9 km s^{-1} in 1 km s^{-1} steps. The colour scale used is shown above, in kelvin. The HH objects known in this region are shown and labelled on the first channel.

profile for this region does indicate some redshifted line wing excess, although there is no corresponding C^{18}O observations towards this position to estimate the central velocity from (and indeed there may not be any C^{18}O emission towards this position). Fig. 23 shows a PV cut along this feature. The bow shock like feature at the end of the outflow can be clearly seen in the bright lobe of redshifted emission in the PV diagram at ~ 1.5 arcmin offset.

C: East and south of SMM 11 by 2.25 arcmin we see a strong blue lobe. It has a minimum velocity of 9 km s^{-1} , with the fastest part of the feature being present at the farthest spatial distance from the main cloud. It does not clearly trace back to any source within the cloud. There is some redshifted emission slightly north and west of this feature, but this appears to connect back further within the cloud.

D: Towards the position of HH 460 we see the end of a strong blueshifted lobe. There is also some much weaker redshifted emission. The maximum blueshifted velocity in this region is at around -11 km s^{-1} .

5.3.2 Extremely high velocity emission

In order to attempt to separate some of this confused outflow structure in this region, we can look at those outflows that have emission at very high velocities – of the order of 10 km s^{-1} away from the line centre. Fig. 21 shows contours of intensity maps of the ^{12}CO data integrated from 24 to 34 km s^{-1} and from -15 to -5 km s^{-1} . These are overlaid on the C^{18}O integrated intensity map. By only looking at the outflows with this extreme velocity range, we are missing out much of the outflowing material in the cloud. However, this reduces the complexity of the velocity structure, and allows us to be fairly confident that we are not including a large amount of ambient emission. This method also allows us to spatially separate otherwise confused and overlapping outflows, and thus calculate properties of specific outflows.

As can be seen in Fig. 21, several regions seem to show compact features around cores, suggesting the presence of outflowing material.

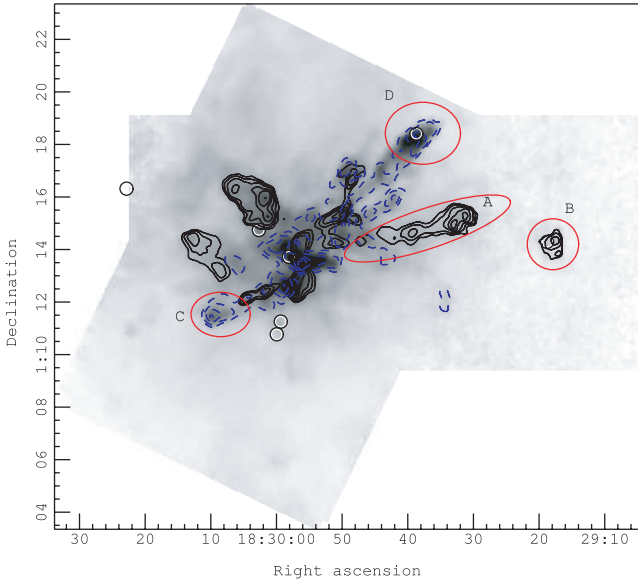


Figure 20. Finder chart for discussion of outflow regions identified from the ^{12}CO channel map in Fig. 19. The regions discussed are shown in the red ellipses labelled A–D. The image shows an integrated ^{12}CO map with red- and blueshifted contours shown as black solid lines and blue-dashed lines, respectively. The HH objects are shown as circles.

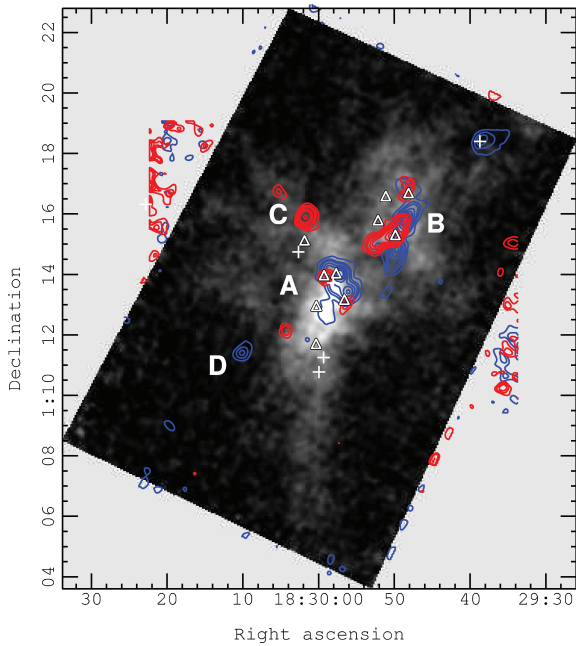


Figure 21. Integrated C^{18}O emission with contours of the highest velocity ^{12}CO emission overlaid. Red contours represent emission from 24 to 34 km s^{-1} , and blue contours represent emission from -15 to -5 km s^{-1} . Positions of the submillimetre cores are shown as white triangles and positions of HH objects are shown as white crosses. Letters label positions of interested discussed below.

A: Specifically around SMM 6, 3 and 4, in the centre of the map, what appears to be at least two overlapping outflows can be seen. The blueshifted contours show two peaks, one at SMM 4 and one around SMM 6 and 3. HH 458 is also centred on this region.

B: SMM 1 and 9 also both show overlapping red and blue lobes, which again appear to belong to two separate outflows. Here the

emission from SMM 1 appears to be much larger than that around SMM 9.

C: There is a strong region of compact redshifted emission to the north of SMM 8; however visual inspection of the ^{12}CO data cube does not reveal any adjacent very-high-velocity blueshifted emission that can be separated from the main line centre emission. The redshifted emission is, however, also near HH 459 so may be connected with that. In the absence of any blueshifted emission it is not possible to identify this feature as indicating a molecular outflow, therefore we have identified this as tentatively connected with the HH object 459, but have not attempted to link it directly to a submillimetre source.

D: South-east of SMM 11 there is some evidence of adjacent red and blue compact regions of emission (in Fig. 21 the blue contoured region is more clearly seen). Inspection of the data cube suggests that the red and blue structure exists more clearly at less extreme velocities. However, given the lack of an obvious source it is not clear whether or not this represent a bipolar outflow. Additionally, inspection of spectra in the redshifted region suggests it is possible that the high-velocity redshifted component may be due to an additional velocity component along the l.o.s. instead of excess line wing emission, so the spatial connection of the red and blue emission may be coincidental. It has not been possible to associate this red/blue region with a submillimetre source.

For the outflows in the SMM 3, 4 and 6 regions and in the SMM 1 and 8 regions we have calculated their properties. As these appear to slightly overlap spatially, it was not possible to perfectly separate these into the four separate outflows we believe exist. Instead, a simple best guess has been taken (on the basis of the contours of the extremely high velocity gas), and spatial regions chosen that appear to contain most of the outflow emission. These spatial regions have then been used to calculate red and blueshifted masses, momentum and kinetic energy for each outflow, using the same assumptions as for the global outflow properties. No attempt has been made to correct for the angle of inclination.

The velocity ranges used in the calculations were -30 to 1.88 km s^{-1} and 17.8 to 36.8 km s^{-1} . The spatial regions were defined separately for the red- and blueshifted emission for each outflow. The masses calculated are shown in Table 3. Again, no attempt was made to correct for inclination.

The total mass for these outflows comes to merely $0.03 M_{\odot}$ for the blueshifted emission and $0.01 M_{\odot}$ for the redshifted emission; this seems low considering the global values we have previously

Table 3. Outflow masses and l.o.s. energetics for ^{12}CO emission in range -30 to 1.8 km s^{-1} (blue) and 17.8 to 36.8 km s^{-1} (red) for each outflow. Note that these outflows are spatially defined on the basis of their extreme velocity emission – closer to the ambient velocity they are spatially substantially larger (and more confused), and the values presented here are very much lower limits for these specific outflows.

	SMM 4	SMM 6 and 3	SMM 1	SMM 8
Mass (M_{\odot})				
Red	0.0061	0.0085	0.012	0.003
Blue	0.0021	0.0016	0.0052	0.0015
Mom ($M_{\odot}\text{ km s}^{-1}$)				
Red	0.0014	0.0012	0.0043	0.0010
Blue	0.0018	0.0028	0.0042	0.00084
Energy ($M_{\odot}\text{ km}^2\text{ s}^{-2}$)				
Red	0.0095	0.0097	0.040	0.0080
Blue	0.012	0.0021	0.034	0.0058

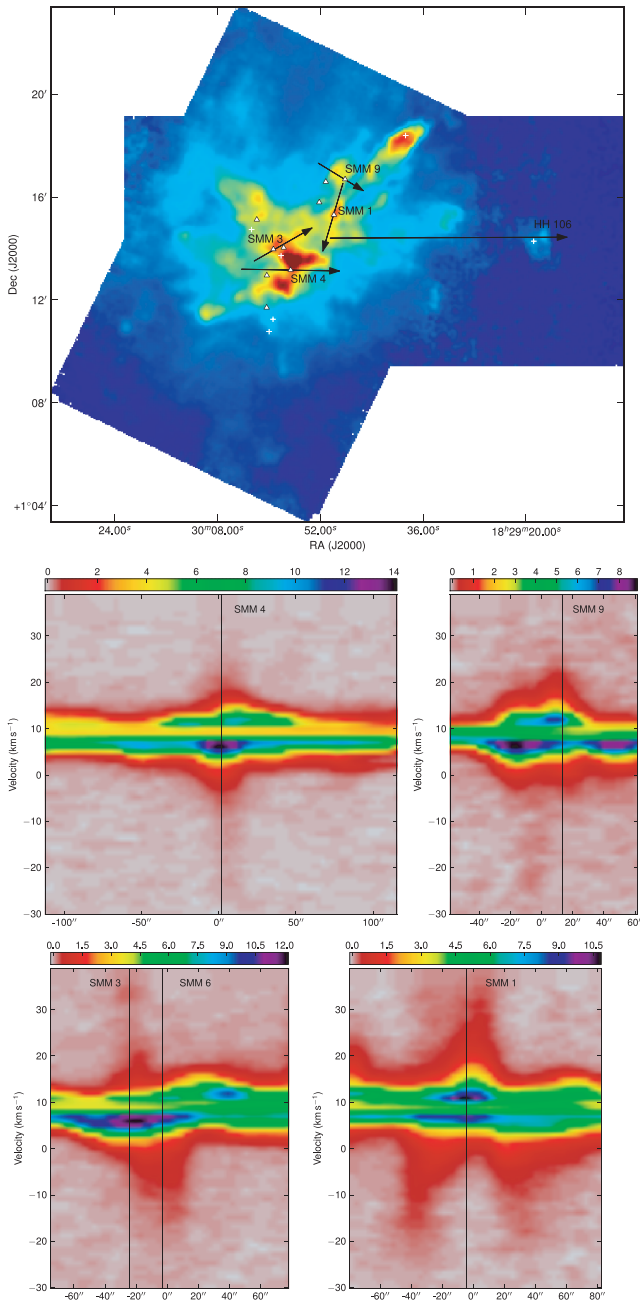


Figure 22. ^{12}CO PV diagrams along the positions of the identified compact outflows, as shown on the integrated image intensity image (top). PV diagrams shown are from SMM 4 (middle left), SMM 9 (middle right), SMM 3 (bottom left) and SMM 1 (bottom right). The position of the appropriate cores is shown as black lines on the PV diagrams. The top image shows the locations of the slices. All intensity values are of T_A^* .

calculated. However, we have been very conservative with the velocity range used here, attempting to be sure that we are not being contaminated by the line centre emission or by overlapping outflows that do not reach such high velocities. If we use the same velocity ranges as used for the global properties then these values approximately double, making these outflows responsible for most of the high-velocity mass in this cloud.

To further show that these outflows are indeed connected with the cores, Fig. 22 shows PV diagrams along the outflows identified. Evidence of the outflow emission can be seen in both the red and

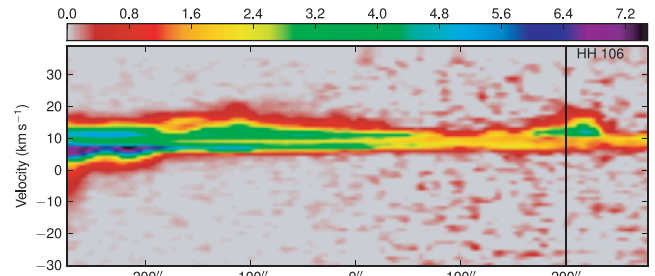


Figure 23. PV diagrams continued from Fig. 22. HH 106: a PV diagram along the long east-west redshifted lobe towards HH 106 is shown.

blueshifted regions, although it is the central line emission that dominates. The dip in the centre of the line shows the self-absorption in the ^{12}CO emission.

6 SUMMARY

High-resolution mapping of the Serpens molecular cloud in the $J = 3 - 2$ transition of ^{12}CO , ^{13}CO and C^{18}O was performed with HARP at the JCMT. The ^{12}CO map traces the numerous outflows in the region, with line wings detected out to -30 and $+37$ km s^{-1} . The C^{18}O map was used to examine the global velocity structure and to estimate the mass of the region, which was found to be $\sim 203 M_{\odot}$. Intensity ratios were also used to estimate an abundance ratio for ^{13}CO to C^{18}O and in turn an estimate of the optical depth. Additionally, the kinetic temperature was examined.

The global velocity structure of Serpens was examined in the C^{18}O emission, and evidence was found to support the conclusion of Duarte-Cabral et al. (2010) that the cloud consists of two sub-clouds at different velocities.

Although across the bulk of the cloud it would not be straightforward to identify the individual outflows present as they overlap spatially, the global properties of the outflowing gas were examined, and we found that the total outflow energy (corrected for random inclination distribution) was approximately 70 per cent of the total turbulent energy in the region. This suggests that the outflows may be a significant factor in driving turbulence in this star-forming region, in broad agreement with many recent simulations and theory.

Four compact outflows towards five of the submillimetre sources were identified on the basis of extremely high velocity emission and their properties examined, finding that this extreme gas does not contribute a large portion of the global outflow energy.

ACKNOWLEDGMENTS

The JCMT is supported by the Science and Technology Facilities Council, the National Research Council Canada and the Netherlands Organisation for Scientific Research.

REFERENCES

- Bastien P., Bissonnette É., Ade P., Pisano G., Savini G., Jenness T., Johnstone D., Matthews B., 2005, *J. R. Astron. Soc. Canada*, 99, 133
- Buckle J. V. et al., 2009, *MNRAS*, 399, 1026
- Buckle J. V. et al., 2010, *MNRAS*, 401, 204
- Carroll J. J., Frank A., Blackman E. G., Cunningham A. J., Quillen A. C., 2009, *ApJ*, 695, 1376
- Casali M. M., Eiroa C., Duncan W. D., 1993, *A&A*, 275, 195
- Curtis E. I., Richer J. S., Buckle J. V., 2010, *MNRAS*, 401, 455
- Davis C. J., Matthews H. E., Ray T. P., Dent W. R. F., Richer J. S., 1999, *MNRAS*, 309, 141

- Davis C. J. et al., 2010, MNRAS, 405, 759
- Di Francesco J., Johnstone D., Kirk H., MacKenzie T., Ledwosinska E., 2008, ApJS, 175, 277
- Duarte-Cabral A., Fuller G. A., Peretto N., Hatchell J., Ladd E. F., Buckle J., Richer J., Graves S., 2010, A&A, 519, A27
- Eiroa C., Djupvik A. A., Casali M. M., 2008, The Serpens Molecular Cloud. Astron. Soc. Pac. Monograph Publications, San Francisco, p. 693
- Evans N. J. et al., 2009, ApJS, 181, 321
- Frerking M. A., Langer W. D., Wilson R. W., 1982, ApJ, 262, 590
- Gregersen E. M., Evans N. J. II, Zhou S., Choi M., 1997, ApJ, 484, 256
- Harvey P., Merín B., Huard T. L., Rebull L. M., Chapman N., Evans N. J. II, Myers P. C., 2007a, ApJ, 663, 1149
- Harvey P. M. et al., 2007b, ApJ, 663, 1139
- Hodapp K. W., 1999, AJ, 118, 1338
- Hogerheijde M. R., van Dishoeck E. F., Salverda J. M., Blake G. A., 1999, ApJ, 513, 350
- Holland W. et al., 2006, Presented at the Society of Photo-Optical Instrumentation Engineers (SPIE) Conference, Vol. 6275, Society of Photo-Optical Instrumentation Engineers (SPIE) Conf. Ser., Bellingham
- Ladd E. F., Fuller G. A., Deane J. R., 1998, ApJ, 495, 871
- Li Z., Nakamura F., 2006, ApJ, 640, L187
- Mac Low M.-M., Klessen R. S., 2004, Rev. Modern Phys., 76, 125
- Matzner C. D., 2007, ApJ, 659, 1394
- McKee C. F., Ostriker E. C., 2007, ARA&A, 45, 565
- McMullin J. P., Mundy L. G., Blake G. A., Wilking B. A., Mangum J. G., Latter W. B., 2000, ApJ, 536, 845
- Moscadelli L., Testi L., Furuya R. S., Goddi C., 2005, Mem. Soc. Astron. Ital., 76, 389
- Myers P. C., 2009, ApJ, 700, 1609
- Olmi L., Testi L., 2002, A&A, 392, 1053
- Rohlfs K., Wilson T. L., 2000, Tools of Radio Astronomy, 3rd edn. Astronomy and Astrophysics Library, Springer-Verlag, Berlin
- Straižys V., Černis K., Bartašiūtė S., 2003, A&A, 405, 585
- Testi L., Sargent A. I., 1998, ApJ, 508, L91
- Ward-Thompson D. et al., 2007, PASP, 119, 855
- White G. J., Casali M. M., Eiroa C., 1995, A&A, 298, 594
- Wilson T. L., Rood R., 1994, ARA&A, 32, 191

This paper has been typeset from a $\text{\TeX}/\text{\LaTeX}$ file prepared by the author.